Analysis and Comparison of the Projectile Impact Response of an Electron Beam Melt-Ti64 Body Centered Cubic Lattice-Cored Sandwich Plate

H. İ. Erten[1] · G. Çimen[1] · F. M. Yıldıztekin[1] · M. Güden[1]

Abstract

Background One potential application of additively fabricated lattice structures is in the blade containment rings of gas turbine engines. The blade containment rings are expected to be able to absorb the kinetic energy of a released blade (broken blade) in order to protect the engine parts from damaging. Metallic lattice-cored sandwich plates provide a gap (free space) between two face sheets, which helps to arrest the released blade and increases the energy absorption capability of containment rings.

Objective The objective was to investigate numerically the projectile impact response of Body-Centered-Cubic (BCC) Electron-Beam-Melt (EBM) lattice-cored/Ti64 face sheet sandwich plates as compared with that of an equal-mass monolithic EBM-Ti64 plate.

Methods The projectile impact simulations were implemented in LS-DYNA using the previously determined flow stress and damage models and a spherical steel impactor at the velocities ranging from 150 to 500 m s^{-1}. The experimental projectile impact tests on the monolithic plate were performed at two different impact velocities and the results were used to confirm the validity of the used flow stress and damage models for the monolithic plate models.

Results Lower impact stresses were found numerically in the sandwich plate as compared with the monolithic plate at the same impact velocity. The bending and multi-cracking of the struts over a wide area in the sandwich plate increased the energy absorption and resulted in the arrest of the projectile at relatively high velocities. While monolithic plate exhibited a local bent area, resulting in the development of high tensile stresses and the projectile perforations at lower velocities.

Conclusions The numerical impact stresses in the sandwich plate were distributed over a wider area around the projectile, leading to the fracture and bending of many individual struts which significantly increased the resistance to the perforation. Hence, the investigated lattice cell topology and cell, strut, and face sheet sizes and the lattice-cored sandwich plate was shown potentially more successful in stopping the projectiles than the equal-mass monolithic plates.

Keywords Electron beam melt · Ti64 · Body centered cubic lattice · Modelling · The Johnson and Cook flow stress and damage model · Projectile impact

Introduction

Metal additive manufacturing (AM) is a relatively new method for manufacturing intricate metallic parts in a near-net shape, with a reduced number of post processing steps and needs for labor [1–4]. Currently, two methods of metal additive manufacturing namely Electron-Beam-Melt (EBM) and Selective Laser Melt (SLM) have been widely investigated for the fabrication of bulk metallic parts and lattice structures. Extremely high cooling rates in both processes (10^3 to 10^8 K/s) [5, 6] result in the development of residual stresses [7–9] and local variations in the microstructure, mechanical properties and defects formed [10–12]. Columnar grains, submicron size cellular structures and the texture development are commonly found in the SLM fabricated 316L [5, 13–21] and AlSiMg [22–26] alloys. The formation of a metastable martensitic phase α' is further observed in

✉ M. Güden
mustafaguden@iyte.edu.tr

1   Dynamic Testing and Modeling Laboratory, Department of Mechanical Engineering, Izmir Institute of Technology, Gülbahçe, Urla, Izmir, Turkey

the SLM- and EBM-Ti64 alloys [27–31]), which increases the strength, but reduces the ductility significantly [32]. The common defects detected in the SLM and EBM processed metallic alloys include gas voids [33], lack of fusions [34] and a high surface roughness caused by the partially melt powder particles at the surfaces [35, 36], which deteriorate the strength and ductility [35, 37, 38].

Besides bulk metallic parts, lattice structures, cellular, reticulated structures constructed by repeating a unit cell made from plates, struts and walls, can be fabricated using the AM methods in various types of intricate topologies with tailored mechanical properties [39]. These structures have high specific peak stresses, bending strengths, energy absorptions, and strength-to-weight ratios [40] and can be designed with multifunctional properties, including impact/blast resistance, heat dissipation, and acoustic isolation [41–43]. The potential applications of additively fabricated metallic lattice structures include the heat exchangers of the integrated anti-icing system of airplanes [44, 45] (increases the cost and energy efficiency and reduces the power consumption); in the walls and ribs of satellites (allows a single lattice design with no bonding) [46]; in the orthopedic implants [47] (improves the biocompatibility and alleviates the stress shielding and energy absorbing structures (makes it possible to mimic crushable natural structures) [48].

One other potential application of lattice structures is in the blade containment rings of gas turbine engines. The blade containment rings are expected to be able to absorb the kinetic energy of a released blade (broken blade) in order to protect the engine parts from damaging [49]. The turbine blade impinges on a circular containment ring at a velocity between 150 and 500 m s^{-1}, usually at an elevated temperature. Various containment materials have been previously investigated, including Inconel 718 [50], aluminum alloys [51], stiffened aluminum plates [52], bilayer structures of aluminum foam, titanium and dry Kevlar fabric [53], shear thickening fluid treated high-strength Kevlar 49 plain weave fabrics [54] and metal/dry plain-woven Kevlar 29 fabric multilayer structure [55]. In a recent study, a bilayer containment ring arrangement, composed of an Al foam layer, a backing dry Kevlar fabric layer and a small gap between them has been shown as an effective containment system [53]. The foam layer absorbed large amount of impact energy and Kevlar fabric resisted the penetration and provided flexibility. The gap between the two layers arrested the released blade, increasing the energy absorption capability of the containment ring. Metallic lattice-cored sandwich structures may replace bilayer containment ring arrangement, as they also provide a gap (free space) between two face sheets. The cell topology and shape and the relative density affect the mechanical properties of lattices and the cell topology and shape also determines the deformation mode under compressive loads (bending-dominated or stretching-dominated).

In the present study, the projectile impact response of an additively processed Body-Centered-Cubic (BCC) lattice-cored/Ti64 face sheet sandwich plate was numerically investigated, as compared with that of an equal-mass monolithic EBM-Ti64 plate. The projectile impact test simulations of the monolithic plate and sandwich plate were implemented using the previously determined flow stress and damage models and a spherical steel impactor at the velocities ranging from 150 to 500 m s^{-1}. The experimental projectile impact tests of the monolithic plates performed at two different impact velocities were further used to confirm the validity of the used flow stress and damage models for the monolithic models.

Materials, Tests and Material Models

Materials

Mechanical test specimens were machined from an EBM fabricated Ti64 plate with the size of 200×70x15 mm and the projectile impact test plates had the size of 150×150x2 mm. These plates were fabricated in an Arcam EBM Q20plus device using Ti64 ELI Grade 5 spherical 30–110 μm powder. The EBM process parameters were as the followings: the beam speed was 40.5 m s^{-1}; the hatch depth was 70 μm; the scanning layer thickness was 90 μm; and the temperature was 750 °C. Figures 1(a) and (b) show the pictures of the as-built 200×70x15 mm and 150×150x2 mm plates, respectively. The scanning strategy in these fabricated plates was a rotating one, ±45° in the building direction/in the X–Y plane (see Fig. 1(a) for the directions). A 3D optical micrograph showing the microstructures in the X-, Y- and Z-direction is shown in Fig. 1(c). The grains are seen columnar in the building Z-direction (110–150 μm) while the grains are nearly equiaxed in the X–Y plane. The details of the microstructural analysis of the phases formed during processing are given elsewhere [56]. Briefly, the microstructure is consisted of α′ (martensite) and α (hcp)+β(bcc).

Projectile Impact Tests

Projectile impact tests on 150×150x2 mm plates (monolithic plates) were performed using a gas-gun set-up as schematically shown in Fig. 2. The set-up is consisted of a gas gun, a barrel and a frame/support fixture. In a typical test, 150×150x2 mm plate with 100×100 impact area (shown in Fig. 1(b)) was fixed on the frame, and a sabot accommodating a steel projectile (12.7 mm in diameter) was propelled by the release of the pressurized air inside the gas gun. A sabot catcher was used to stop the sabot at the exit of the barrel. The projectile velocities before and

Fig. 1 The pictures and sizes of EBM-Ti64 plates: (a) 15 mm-thick plate used for the mechanical tests and (b) 2 mm-thick projectile impact tested plate and (c) 3D optical micrograph showing the microstructures in the Z- (building direction), Y- and X-direction
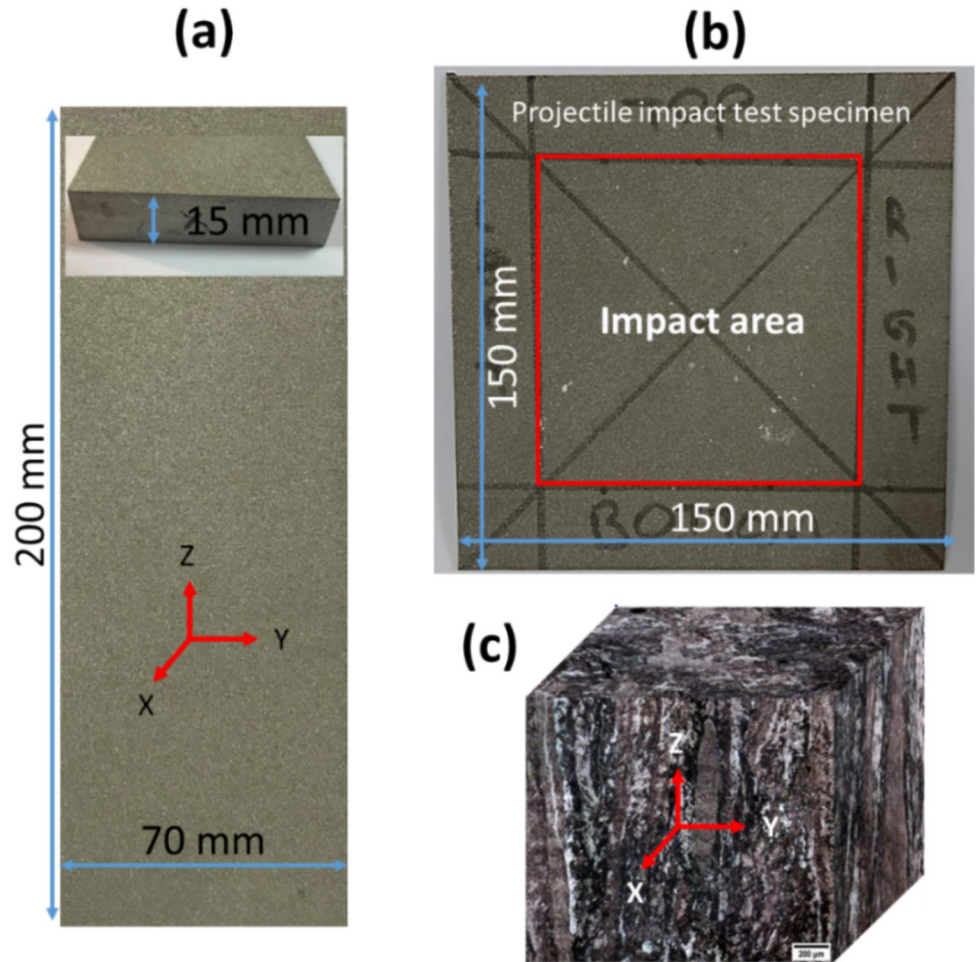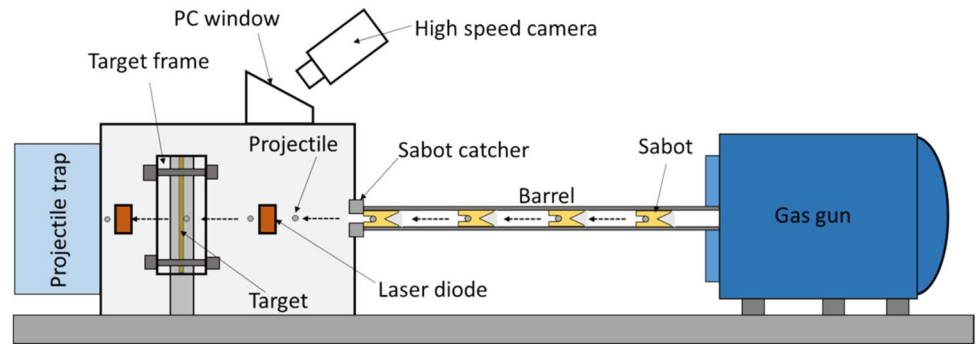

Fig. 2 The schematic of the projectile impact test set-up

after the impact (perforation) were measured using laser velocity sensors. A high-speed Photron SA1.1 FASTCAM camera was used to record the deformation at 20,000 fps. The tests were performed at the projectile impact velocities of 150 and 230 m s^{-1}. A plug was formed at the back of the plates in the case of perforation (230 m s^{-1}). This resulted in an earlier trigger of the laser sensor. In these tests, the high speed camera was used to determine the exit velocity of the projectiles.

Numerical Models of the Projectile Impact Tests

The monolithic plate and BCC lattice-cored sandwich plate projectile impact responses were simulated at the velocities ranging from 150 to 500 m s^{-1} in LS-DYNA. The model geometries of the monolithic plate and BCC lattice-cored sandwich plate with the projectile are shown in Fig. 3. The numerical projectile had a diameter of 12.7 mm, the same as the experiments. In the simulations, the projectile was modelled linear elastic using the constant stress solid elements
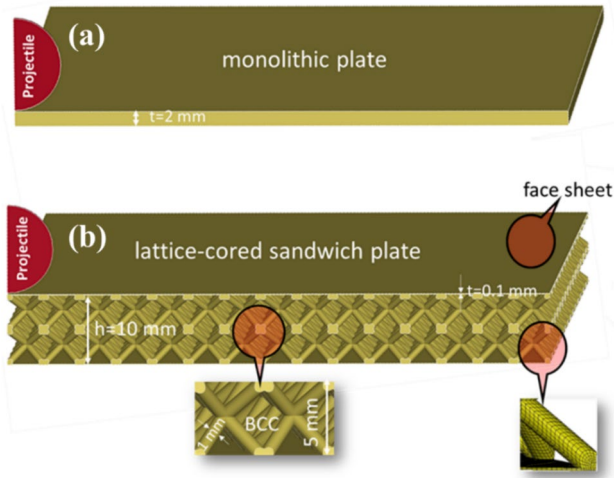
Fig. 3 Quarter models of EBM-Ti64 (a) monolithic plate and (b) lattice-cored sandwich plate

with the following mechanical properties: E = 210 GPa, ρ = 7800 kg m^{-3} and v = 0.33 [57]. The monolithic plate and lattice-cored sandwich plate were modelled in quarter with a cross-section of 150 mm. The impact area of both plates was 100 × 100 mm and out of the impact area of the plates and sandwiches was fully constrained, as similar with the monolithic plate projectile impact tests. The thickness of the monolithic plate was 2 mm and the lattice-core structure was 10 mm with a 0.1 mm-thick face sheet at both faces. The BCC core had a strut diameter of 1 mm, a cell size of 5 mm and a relative density of 0.18. The thicknesses of the lattice-cored and the face sheet were selected as such that sandwich and monolithic plate had equal mass. Both plates were modelled with the constant stress solid hexahedral elements and the Flanagan-Belytschko stiffness for hourglass. The contacts in the lattice were AUTOMATIC_SINGLE_SURFACE and the contact between the lattice and projectile was ERODING_SURFACE_TO_SURFACE, as with the contact between monolithic plate and projectile. A mesh sensitivity analysis was performed in the projectile impact test models of the monolithic plate at the impact velocity of 230 m s^{-1} using 0.25, 0.4, 0.6 and 0.8 mm mesh sizes.

Monolithic and sandwich plates were modelled using the Johnson–Cook (JC) flow stress and damage models (MAT15

in LS-DYNA). The flow stress σ_y in the JC flow stress model is [58]

$$\sigma_y = \left(A + B\varepsilon_{ep}^n\right)\left[1 + cln(\dot{\varepsilon}^*)\right]\left[1 - (T^*)^m\right] \qquad (1)$$

where, A, B, n, c, and m are sequentially the yield stress, hardening modulus, strain hardening coefficient, strain rate sensitivity, and thermal softening parameters, $\dot{\varepsilon}^* = \left(\frac{\dot{\varepsilon}_{ep}}{\dot{\varepsilon}_0}\right)$; where ε_{ep}, $\dot{\varepsilon}_{ep}$ and $\dot{\varepsilon}_0$ are sequentially the equivalent plastic strain, strain rate and reference strain rate; $T^* = \left(\frac{T-T_r}{T_m-T_r}\right)$; where T is the temperature, T_m is the melting temperature, and T_r is the reference or room temperature. The plastic strain at fracture (ε_{pf}) in the JC damage model is [59]

$$\varepsilon_{pf} = \left[D_1 + D_2e^{D_3\sigma^*}\right]\left[1 + D_4ln(\varepsilon^*)\right]\left[1 + D_5T^*\right] \qquad (2)$$

where, D_1-D_5 are the parameters determined experimentally and σ^* is the stress triaxiality, which is $\frac{\sigma_h}{\sigma_e}$; where σ_h is the hydrostatic stress and σ_e is the equivalent stress.

In a previous study [56], the JC flow stress (A, B, n and c) and damage model (D_1-D_5) parameters of the investigated EBM-Ti64 monolithic plate were determined using the quasi-static and high strain rate tension tests on the machined standard tension test specimens and a strut based micro compression test was used to determine the lattice material flow stress parameters. The determined flow stress and damage model parameters of both monolithic plate and strut are tabulated in Table 1. A thermal softening parameter of m = 1 was used in the models [60, 61]. Although the damage model parameters of the monolithic plate and strut were shown similar through modelling, the JC flow stresses of struts were found to be lower than those of the machined bulk tension specimens [56] (see Figs. 4(a) and (b)). Some what a similar result was reported in a previous study [62]. The surface machining increased the flow stresses of an as-built EBM-Ti64 by 85–95 MPa without altering the failure strains. In another study, tensile tests were performed on small size diameter (0.81 mm) and standard size diameter (8.8 mm) SML-316 test specimens and it was shown that small-diameter samples exhibited ~ 200 MPa lower flow stresses [63]. This was ascribed to the variations between the microstructures of mini- and standard-specimens due to the involvement of different thermal gradients and

Table 1 The determined flow stress and damage model parameters of plate and strut [56]

	A (MPa)	B (MPa)	n	c	m	T_m (°C)	ρ (kg m^{-3})	ν	E (GPa)
Plate	937	556	0.35	0.012	1	1653	4350	0.3	117
Strut	800	663	0.49	0.012	1	1653	4350	0.3	117
	D_1	D_2	D_3	D_4	D_5	$\dot{\varepsilon}_0$(s^{-1})			
Plate	0.1	0.142	−1.5	0	0	0.001			
Strut	0.1	0.142	−1.5	0	0	0.001			

Fig. 4 The JC flow stress model true stress-true plastic strain curves (a) the plate and (b) strut and the fracture strain variation with (c) stress triaxiality and (d) strain rate (redrawn from [56])
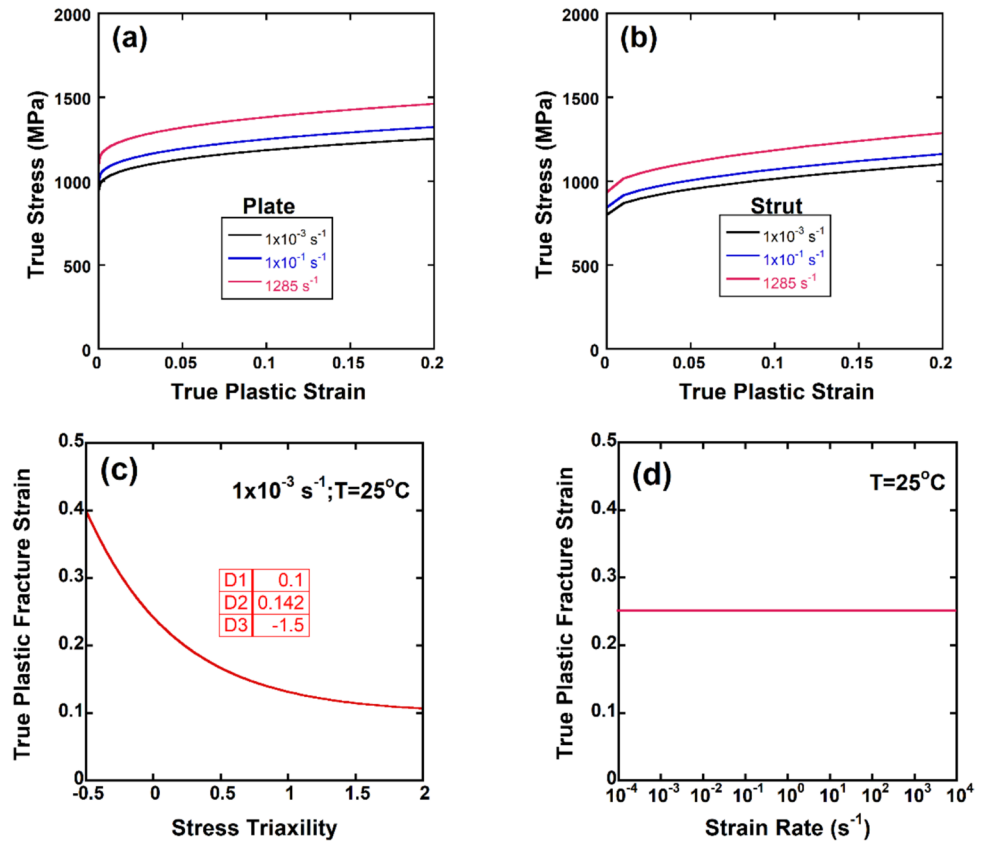
temperature histories during manufacturing. The plate flow stress parameters listed in Table 1 were used to model the projectile impact tests of the investigated EBM-Ti64 plates and the strut flow stress parameters were used to model the projectile impact test models of the investigated lattice-cored sandwich plates in the present study. The equivalent true plastic fracture strain variation with the stress triaxiality is shown in Fig. 4(c). Although the fracture strain exhibits a notch sensitivity, no trend in the fracture strain is seen with strain rate (Fig. 4(d)). Note also that high strain rate tests are near adiabatic, which means that the specimen is heated during deformation. It was stated that the values D_4 and D_5 were coupled and both values approached zero [56]. As the LS-DYNA MAT15 [64] takes into account the adiabatic heating thorough the internal energy and heat capacity (specific heat capacity = 520 kJ kg^{-1} ^{o}C^{-1} [65]), the heating effect during projectile impact was included in the simulations.

The validity of determined damage model parameters was shown previously through the quasi-static compression testing of $4 \times 4x4$ EBM-Ti64 BCC lattices having a 10 mm cell size and a 2 mm strut size [56]. The use of plate flow stress model parameters together with the plate damage model parameters resulted in higher numerical initial crushing stresses than that of experiments, on the other side, the use of the strut flow stress model with the plate damage model predicted similar crushing stresses and strut crushing

behavior with the experiments. Therefore, the projectile impact models of the sandwich plates were implemented using the strut flow stress model.

Results and Discussion

The projectile velocity versus time curves of the projectile impact models of the monolithic plate at the impact velocity of 230 m s^{-1} using different mesh sizes are shown in Fig. 5. Although the projectile perforates the monolithic plate in all models, the mesh size significantly alters the projectile exit times and velocities. Decreasing mesh size from 0.8 mm to 0.25 mm, as seen in Fig. 5, increases the exit velocity from 83 m s^{-1} to 110 m s^{-1} and decreases the exit time from 105 µs to 85 µs. The reduction of mesh size from 0.4 mm to 0.25 mm, on the other side, changes the exit time and velocity slightly, 0.1%. A mesh convergence at nearly 0.4 mm is therefore determined after the analysis while the models were continued using the 0.25 mm mesh size due to relatively small strut diameter, 1 mm, used in the lattice.

The final deformed pictures of monolithic plates after the impact at different projectile velocities are shown in Fig. 6. The projectile bends the plate at the mid-section and forms an indent/cracks at the front surface of the plate without penetration/perforation at 150 m s^{-1}. The projectile, however,
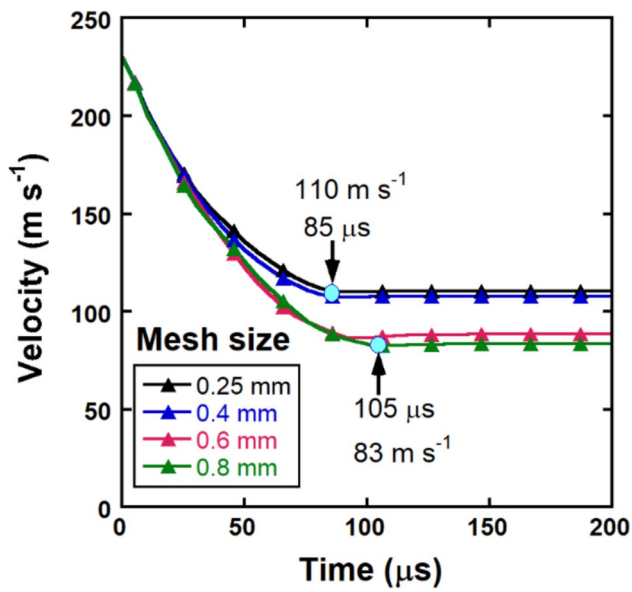
Fig. 5 The numerical projectile velocity versus time of the projectile impact test of EBM- Ti64 monolithic plate at 230 m s^{-1}

perforates the plate at 230, 300, 400 and 500 m s^{-1}, cracking the plate in few pieces at the impact location after the perforation.

Figures 7(a) and (b) show the numerical and experimental deformation time histories of the monolithic plate at 150 and 230 m s^{-1}. At the lowest projectile velocity of 150 m s^{-1}, the projectile induces a small crack at the impact location of the plate numerically while no visible damage is seen experimentally at the impact surface but a small crack propagating at the back side of the plate is observed (see Fig. 7(a), the last picture). At this velocity, the projectile is bounced back after the impact both numerically and experimentally (Fig. 7(a)). When the velocity increases to 230 m s^{-1}, the projectile perforates the plate both numerically and experimentally as seen in Fig. 7(b). After the perforation (at 500 μs), a cracked section (hole) around the impact location is formed, the size of which is very similar to the diameter of the projectile both numerically and experimentally (Fig. 7(b)). Above comparison between the model and experiments shows that the used flow stress and damage model parameters nearly predict the projectile impact
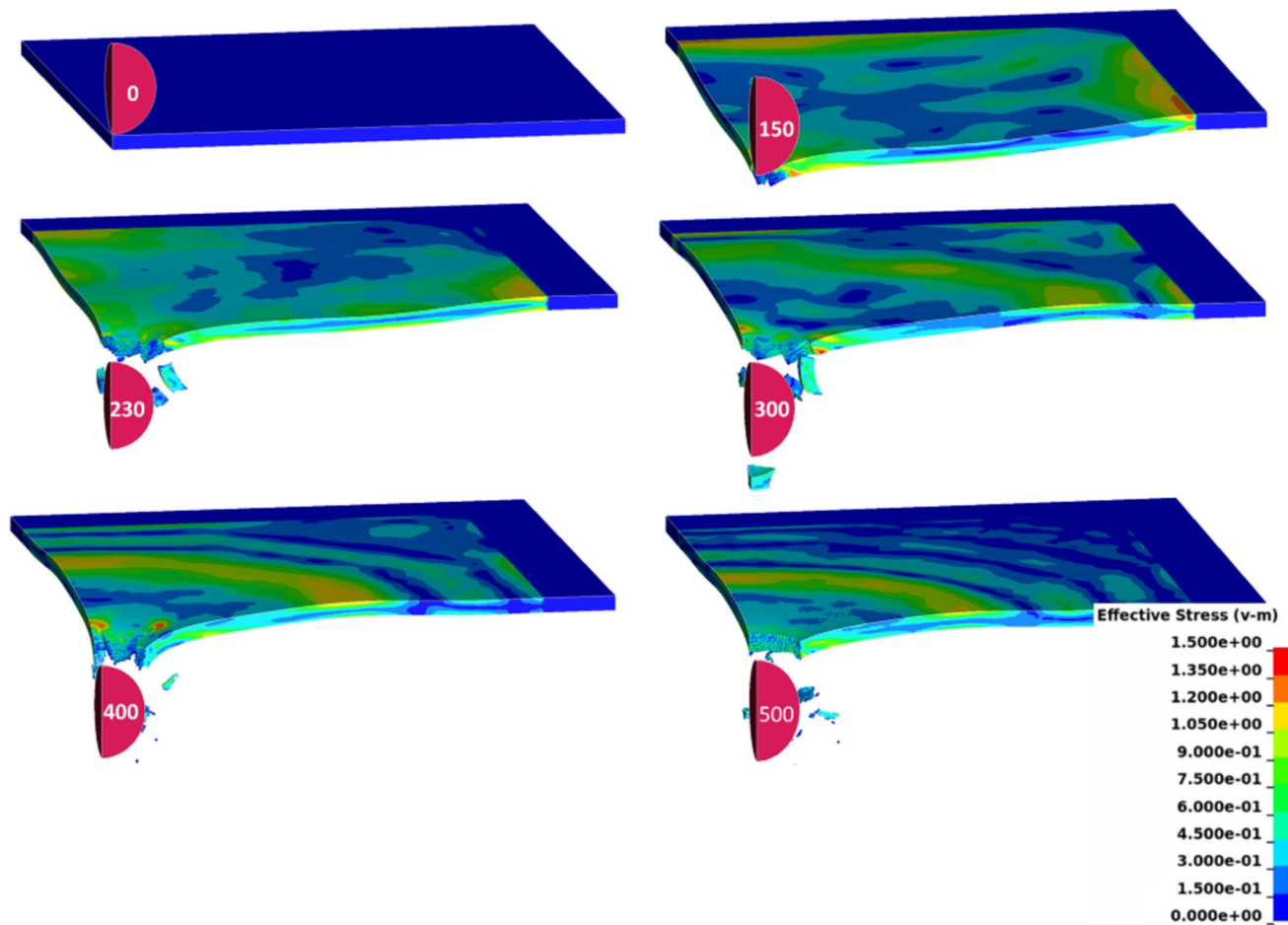

Fig. 6 The numerical final deformation pictures of EBM-Ti64 monolithic plate at different impact velocities (numbers show the initial projectile velocity)
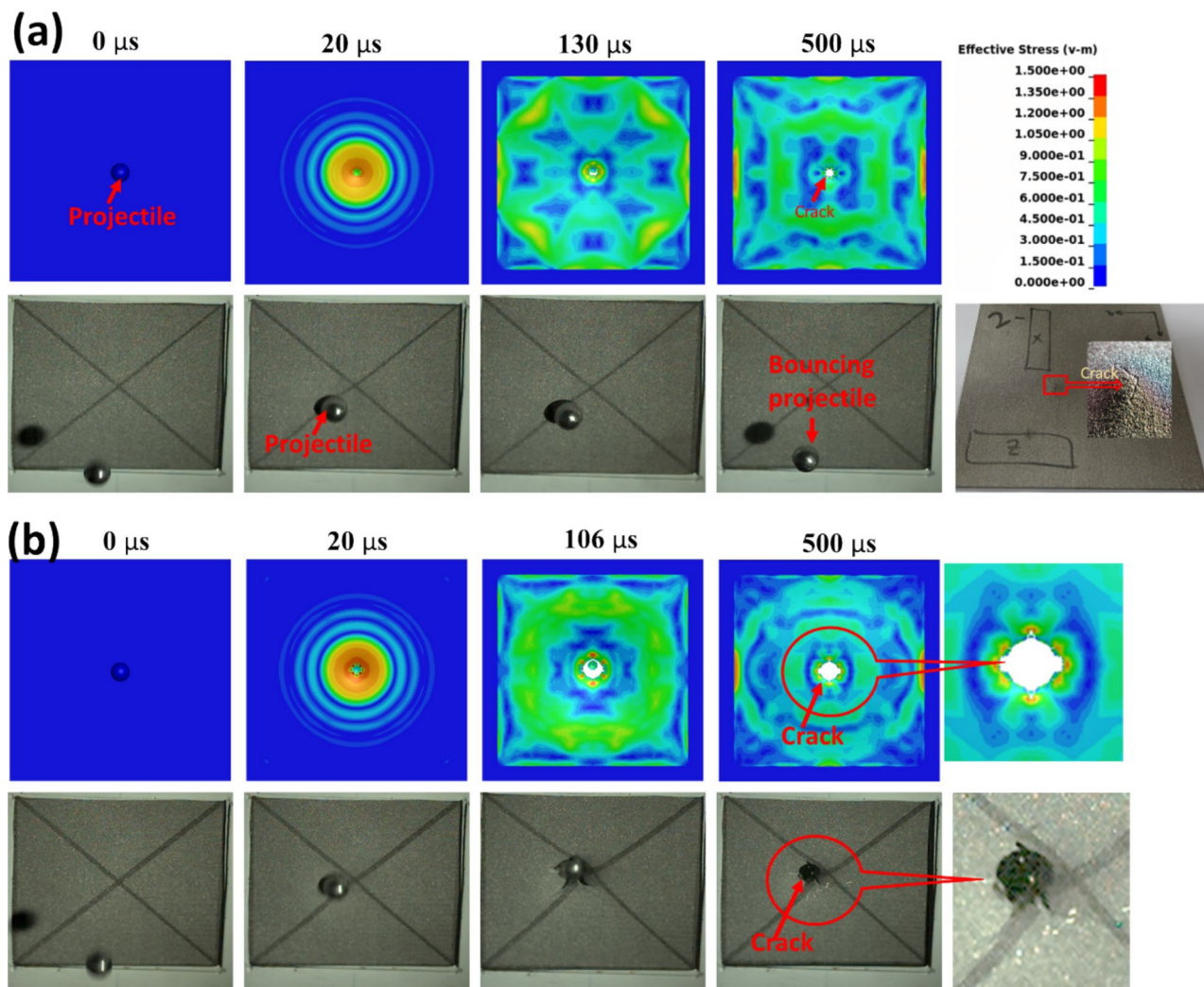
Fig. 7 The projectile impact numerical and experimental deformation pictures of monolithic plate at different times at the impact velocities of (a) 150 m s^{-1} and (b) 230 m s^{-1}

damage formation at two different velocities in EBM-Ti64 monolithic plates. The numerical cracking of the plate at the impacted side and experimental no surface cracking but back surface cracking at 150 m s^{-1} are ascribed to the anisotropic behavior of the EBM-Ti64 monolithic plate, which may be slightly stronger and more brittle in the Z-direction. The exit velocity was measured 107 m s^{-1} in the experiment while 110 m s^{-1} in the model. This result concludes a slightly more brittle behavior of the experimental plate. Since the main aim of the present study is to investigate the projectile impact response of the lattice-cored sandwich plate as compared with that of an equal-mass monolithic plate, this discrepancy between the model and experiment is omitted.

The final deformed pictures of the EBM-Ti64 lattice-cored sandwich plates after the projectile impact at different impact velocities are shown in Fig. 8. As seen in the same figure, the projectile penetrates the lattice core until

about 400 m s^{-1} without perforation. The perforation of the projectile starts after about above 400 m s^{-1} and EBM-Ti64 lattice-cored sandwich plate is perforated at both 450 and 500 m s^{-1} impact velocities as seen in Fig. 8. The deformation in the sandwich plate proceeds with face sheet deformation/cracking and strut bending and fracture locally as also seen in the same figure.

Figure 9 shows the numerical deformation history pictures of monolithic plate and sandwich plate at 450 m s^{-1} velocity, at which both plates are perforated. One clear difference in the deformation behavior between monolithic plate and lattice-cored sandwich, as seen in the same figure, is that the monolithic plate exhibits a local bent area at this velocity while almost no global bending is seen in the lattice-cored sandwich plate. The local bending leads to the development of high tensile, compression and shear stresses through the thickness of the plate. The high tensile
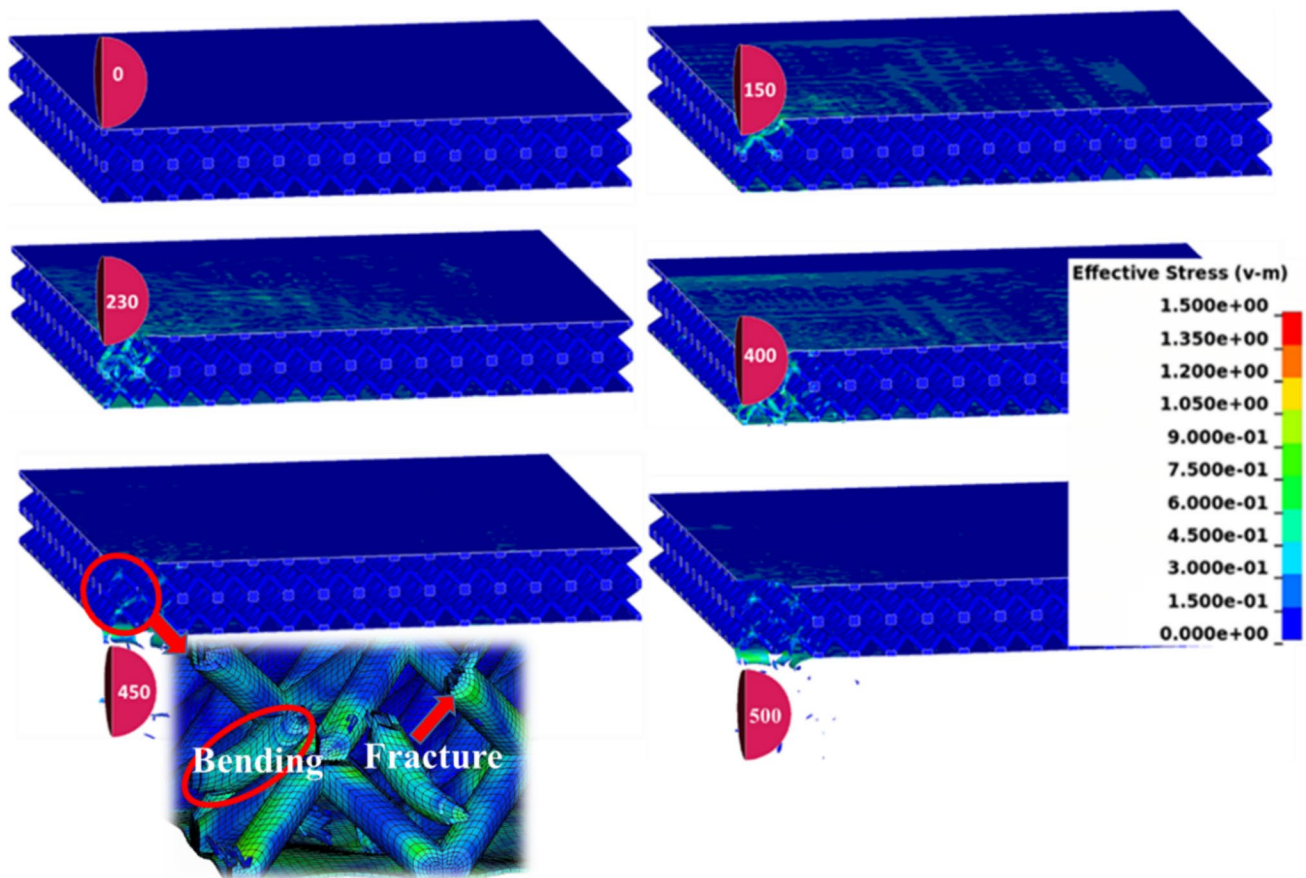
Fig. 8 The numerical final deformation pictures of EBM-Ti64 lattice-cored sandwich plate at different impact velocities (numbers show the initial projectile velocity)

stresses at the distal end of the plate, as marked by the filled arrows in Fig. 10, develops tension cracks at distal end. As stated earlier, the deformation of the sandwich plate however proceeds mainly with the bending and fracture of individual struts in contact with the projectile. The stresses in the sandwich plate are also distributed to a wider area around the projectile as marked by the open arrows in Fig. 10. This stress distribution delays the perforation in the sandwich plate as compared with the monolithic plate.

The pictures of the numerical deformation history of the sandwich plate and monolithic plate impacted at 400 m s^{-1} are shown in Fig. 11, for a comparison. The projectile velocity versus time curves of monolithic plate and lattice-core sandwich plate are further shown in Figs. 12(a) and (b), respectively. The sandwich plate arrests the projectile at about 60 μs at 400 m s^{-1} (Fig. 12(b)) while the monolithic plate is perforated by the projectile (Fig. 12(a)). Until about 60 μs arrest time, the sequences of sandwich core deformation are clearly seen in Fig. 11. The impact of projectile initially deforms/fractures the face sheet after 5 μs, at the same time, the struts underneath the projectile are stressed and few are also cracked locally. As the projectile penetrates the

sandwich plate (15 μs), the stress is transferred to the horizontal and vertical struts. As compared with the monolithic plate, the maximum effective stress in the sandwich plate is much lower as seen in Fig. 11. The bending and fracture of many struts at the impact location are seen at 40 μs and the fracture/cracking of struts occurs both at the nodal points and along the strut length. This bending and multi-cracking feature of the sandwich plate increase the energy absorption and result in the arrest of the projectile. As seen in Fig. 12, the projectile exit velocity increases and exit time decreases as the initial projectile velocity increases. The velocity of the projectile in the sandwich plate seen in Fig. 12(b) quickly declines to zero in $50-100$ μs after the impact at the impact velocities between 150 and 400 m s^{-1}.

The present study shows that the numerical perforation resistance of lattice-cored sandwich plate increased as compared with the monolithic plate. A simple lattice structure of BCC was selected for the present study with a relative density of 0.18, a strut diameter of 1 mm and a unit cell of 5 mm. The use of more complex lattice structures with direction dependent mechanical properties may however result in different results. Few lattices also show
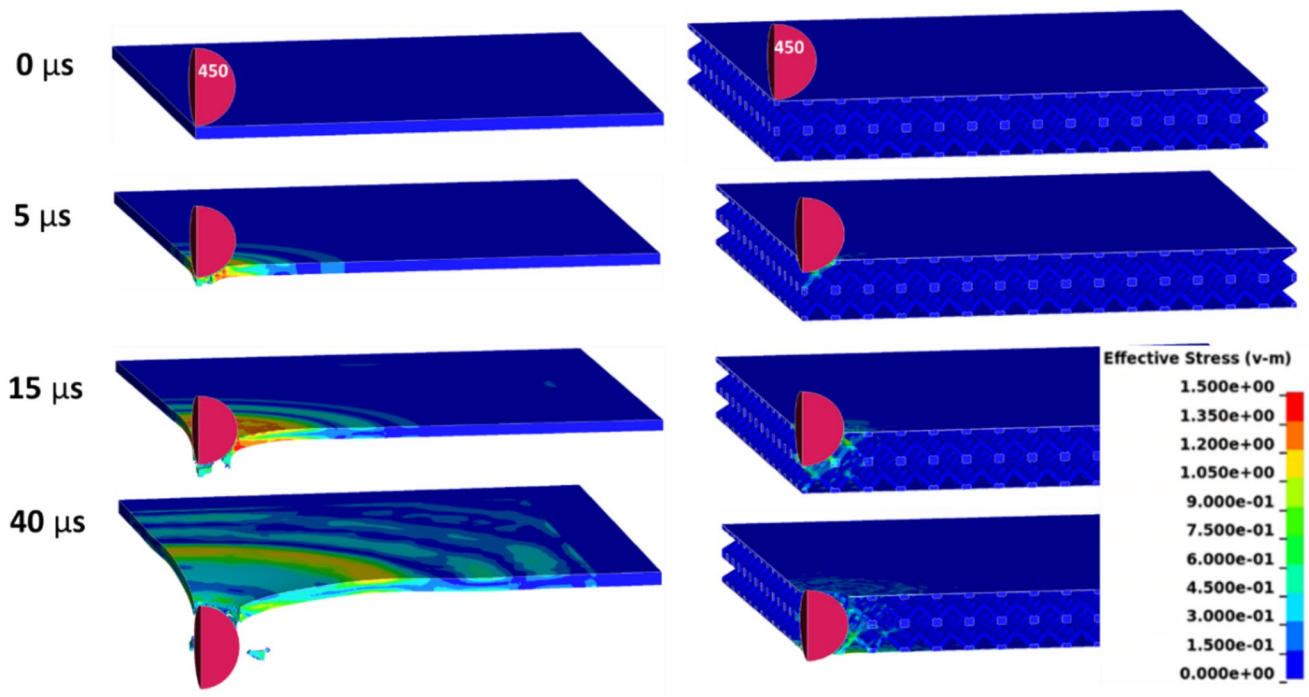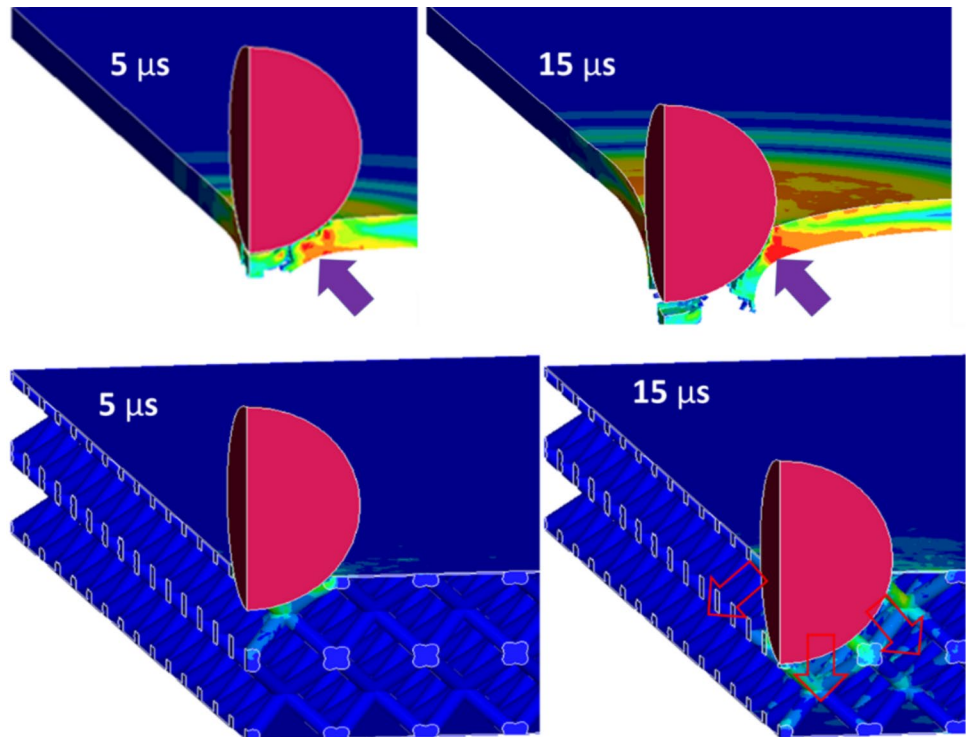
Fig. 9 The numerical deformation pictures of monolithic plate and sandwich plate at 450 m s^{-1}

Fig. 10 The magnified numerical deformation pictures of monolithic plate and sandwich plate at 5 and 15 μs (450 m s^{-1})

a stretching-dominated deformation in which the strength increases significantly over the bending-dominated lattices. The Maxwell criterion [66] is further used for the classification either as bending-dominated or stretching-dominated

$$M = b - 3j + 6 \tag{3}$$

where b is the number of struts and j is the number of joints. The value of M is less than zero for bending-dominated and
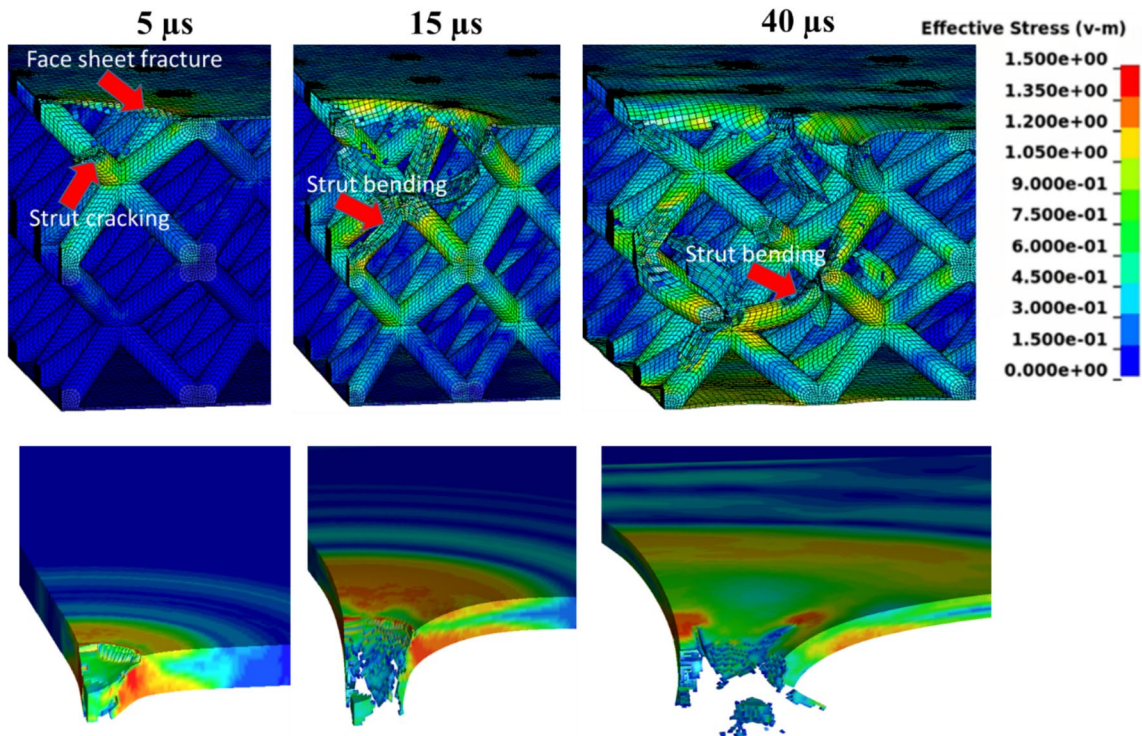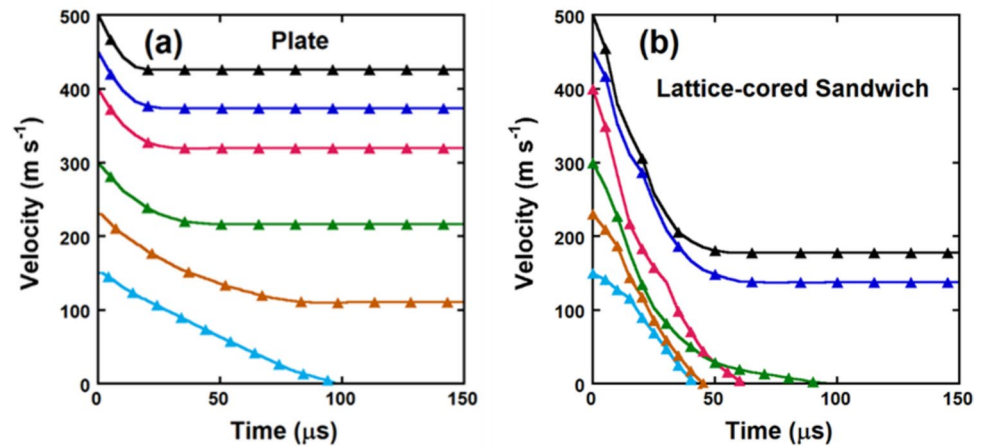
Fig. 11 The deformation of sandwich plate and monolithic plate at 5, 15 and 40 μs (400 m s^{-1})

Fig. 12 The projectile velocity versus time curves of (a) monolithic plate and (b) lattice-cored sandwich plate

either zero or greater than zero for stretching-dominated deformation. The criterion in terms of cell connectivity (Z) is the following: if the number of connectivity is less than 12, the deformation is bending-dominated, and if the number is equal to or higher than 12, it is stretching-dominated [67]. The BCC lattice with 8 connectivity; therefore, is bending-dominated while the FCC lattice with 12 connectivity is stretching-dominated. Further studies will focus on the use of stretching-dominated lattice structures with varying cell size and strut diameter and length.

The processing of 0.1 mm thick face sheets additively is a challenge using the currently available additive machines.

One possible way is to braze the conventionally produced thin face sheets to the additively processed BCC cores. However, brazing at an elevated temperature may induce thermal warpage on the face sheets and core. Another option is to fabricate the sandwich plates with thicker face sheets and then reduce the thickness of face sheets through machining. Both will be investigated as future studies. Furthermore, the sandwich face sheets were modelled using the strut model. In real applications, a separate material model for the face sheets may be needed in order to increase the fidelity of the numerical approach used here.

Conclusion

In the present study, the projectile impact response of equal-mass EBM-Ti64 monolithic plate and BCC lattice-cored sandwich plate were numerically investigated and compared. The impact models were simulated using the previously determined JC flow stress and damage models. The experimental projectile impact tests of monolithic plates confirmed the validity of the used material models. The results showed that the lattice-cored sandwich plate was more effective in stopping the projectiles than the monolithic plates for the studied lattice cell topology and cell, strut and face sheet size. The tensile stresses formed at the back side of monolithic plates resulted in the cracking of the plate at relatively low velocities. The impact stresses in the sandwich plate were however found to be distributed over a wider area around the projectile, leading to the fracture and bending of many individual struts which significantly increased the resistance to the perforation.

Data Availability The raw/processed data required to reproduce these findings cannot be shared at this time as the data also forms part of an ongoing study.

Declarations

Conflicts of Interest The authors declare no conflict of interest.

References

1. Gite RE, Wakchaure VD (2023) A review on process parameters, microstructure and mechanical properties of additively manufactured AlSi10Mg alloy. Mater Today: Proc 72:966–986
2. Distefano F, Pasta S, Epasto G (2023) Titanium Lattice Structures Produced via Additive Manufacturing for a Bone Scaffold: A Review. J Funct Biomater 14(3):125
3. Isaac CW, Duddeck F (2022) Current trends in additively manufactured (3D printed) energy absorbing structures for crashworthiness application – a review. Virtual Phys Prototyp 17(4):1058–1101
4. Haghdadi N et al (2020) Additive manufacturing of steels: a review of achievements and challenges. J Mater Sci 56(1):64–107
5. Song B et al (2015) Differences in microstructure and properties between selective laser melting and traditional manufacturing for fabrication of metal parts: A review. Front Mech Eng 10(2):111–125
6. Loh L-E et al (2015) Numerical investigation and an effective modelling on the Selective Laser Melting (SLM) process with aluminium alloy 6061. Int J Heat Mass Transf 80:288–300
7. Mercelis P, Kruth JP (2006) Residual stresses in selective laser sintering and selective laser melting. Rapid Prototyp J 12(5):254–265
8. Fang ZC et al (2020) Review on residual stress in selective laser melting additive manufacturing of alloy parts. Opt Laser Technol 129:15
9. Kim T et al (2019) Analysis of residual stress evolution during powder bed fusionprocess of AISI 316L stainless steel with experiment and numerical modeling. Int J Adv Manuf Technol 105(1–4):309–323
10. Fayazfar H et al (2018) A critical review of powder-based additive manufacturing of ferrous alloys: Process parameters, microstructure and mechanical properties. Mater Des 144:98–128
11. Bajaj P et al (2020) Steels in additive manufacturing: A review of their microstructure and properties. Mater Sci Eng a-Struct Mater Prop Microstruct Proc 772:25
12. Lewandowski JJ, Seifi M (2016) Metal Additive Manufacturing: A Review of Mechanical Properties. In: Clarke DR (ed) Annual Review of Materials Research, vol 46. Annual Reviews, Palo Alto, pp 151–186
13. Saeidi K et al (2015) Hardened austenite steel with columnar sub-grain structure formed by laser melting. Mater Sci Eng a-Struct Mater Prop Microstruct Proc 625:221–229
14. Zhong Y et al (2016) Intragranular cellular segregation network structure strengthening 316L stainless steel prepared by selective laser melting. J Nucl Mater 470:170–178
15. Zietala M et al (2016) The microstructure, mechanical properties and corrosion resistance of 316 L stainless steel fabricated using laser engineered net shaping. Mater Sci Eng a-Struct Mater Prop Microstruct Proc 677:1–10
16. Sun Z et al (2018) Simultaneously enhanced strength and ductility for 3D-printed stainless steel 316L by selective laser melting. NPG Asia Mater 10(4):127–136
17. Sun S-H et al (2019) Excellent mechanical and corrosion properties of austenitic stainless steel with a unique crystallographic lamellar microstructure via selective laser melting. Scripta Mater 159:89–93
18. Niendorf T et al (2014) Functionally Graded Alloys Obtained by Additive Manufacturing. Adv Eng Mater 16(7):857–861
19. Andreau O et al (2019) Texture control of 316L parts by modulation of the melt pool morphology in selective laser melting. J Mater Process Technol 264:21–31
20. Dallago M et al (2019) On the effect of geometrical imperfections and defects on the fatigue strength of cellular lattice structures additively manufactured via Selective Laser Melting. Int J Fatigue 124:348–360
21. Niendorf T et al (2013) Highly Anisotropic Steel Processed by Selective Laser Melting. Metall and Mater Trans B 44(4):794–796
22. Jing C et al (2020) Microstructure, porosity and mechanical properties of selective laser melted AlSi10Mg. Chin J Aeronaut 33(7):2043–2054

23. Rometsch PA et al (2022) Review of high-strength aluminium alloys for additive manufacturing by laser powder bed fusion. Mater Des 219:110779

24. Cabibbo M et al (2022) Mechanical spectroscopy study of as-cast and additive manufactured AlSi10Mg. J Alloy Compd 914:165361

25. Shakil S et al (2021) Additive manufactured versus cast AlSi10Mg alloy: Microstructure and micromechanics. Results Mater 10:100178

26. Hadadzadeh A et al (2021) Microstructural consistency in the additive manufactured metallic materials: A study on the laser powder bed fusion of AlSi10Mg. Addit Manuf 46:102166

27. Zafari A, Xia K (2018) High Ductility in a fully martensitic microstructure: a paradox in a Ti alloy produced by selective laser melting. Mater Res Lett 6(11):627–633

28. Lekoadi P et al (2021) Evaluation of heat treatment parameters on microstructure and hardness properties of high-speed selective laser melted ti6al4v. Metals 11(2):1–15

29. Yang J et al (2017) Effect of crystallographic orientation on mechanical anisotropy of selective laser melted Ti-6Al-4V alloy. Mater Charact 127:137–145

30. Tan X et al (2016) Revealing martensitic transformation and α/β interface evolution in electron beam melting three-dimensional-printed Ti-6Al-4V. Sci Rep 6(1):26039

31. Panin A et al (2019) Microstructure and mechanical behaviour of additive manufactured Ti–6Al–4V parts under tension. In EPJ Web of Conferences. EDP Sciences.

32. Jamhari FI et al (2023) Influence of Heat Treatment Parameters on Microstructure and Mechanical Performance of Titanium Alloy: A Brief Review. J Mater Res Technol 24:4091

33. Grasso M, Colosimo BM (2017) Process defects and <i>in situ</i> monitoring methods in metal powder bed fusion: a review. Meas Sci Technol 28(4):044005

34. Ladewig A et al (2016) Influence of the shielding gas flow on the removal of process by-products in the selective laser melting process. Addit Manuf 10:1–9

35. Rafi HK et al (2013) Microstructures and Mechanical Properties of Ti6Al4V Parts Fabricated by Selective Laser Melting and Electron Beam Melting. J Mater Eng Perform 22(12):3872–3883

36. Chern AH et al (2019) A review on the fatigue behavior of Ti-6Al-4V fabricated by electron beam melting additive manufacturing. Int J Fatigue 119:173–184

37. de Formanoir C et al (2016) Electron beam melted Ti–6Al–4V: Microstructure, texture and mechanical behavior of the as-built and heat-treated material. Mater Sci Eng, A 652:105–119

38. Masuo H et al (2018) Influence of defects, surface roughness and HIP on the fatigue strength of Ti-6Al-4V manufactured by additive manufacturing. Int J Fatigue 117:163–179

39. Zhang XZ et al (2018) Selective electron beam manufactured Ti-6Al-4V lattice structures for orthopedic implant applications: Current status and outstanding challenges. Curr Opin Solid State Mater Sci 22(3):75–99

40. Zhu L, Li N, Childs PRN (2018) Light-weighting in aerospace component and system design. Propulsion Power Res 7(2):103–119

41. Gibson, L.J. and M.F. Ashby, *Cellular Solids: Structure and Properties*. 2 ed. Cambridge Solid State Science Series. 1997, Cambridge: Cambridge University Press.

42. Evans AG et al (2001) The topological design of multifunctional cellular metals. Prog Mater Sci 46(3–4):309–327

43. Evans A (1998) Multifunctionality of cellular metal systems. Prog Mater Sci 43(3):171–221

44. Careri F et al (2023) Additive manufacturing of heat exchangers in aerospace applications: a review. Appl Therm Eng 235:121387

45. Ferro CG, Pietrangelo F, Maggiore P (2023) Heat exchange performance evaluation inside a lattice panel using CFD analysis for an innovative aerospace anti-icing system. Aerosp Sci Technol 141:108565

46. Boschetto A et al (2023) Additive Manufacturing for Light-weighting Satellite Platform. Appl Sci 13(5):2809

47. Tyagi SA, Manjaiah M (2023) Additive manufacturing of titanium-based lattice structures for medical applications – A review. Bioprinting 30:e00267

48. Ramakrishna D, BalaMurali G (2023) *Bio-inspired 3D-printed lattice structures for energy absorption applications: A review.* Proceedings of the Institution of Mechanical Engineers. Part L J Mater Design Appl 237(3):503–542

49. Roy PA, Meguid SA (2021) Containment of blade shedding in gas turbine engines: part I-design and development of a scaled down test rig. Int J Mech Mater Des 17(1):3–12

50. Pereira JM, Lerch BA (2001) Effects of heat treatment on the ballistic impact properties of Inconel 718 for jet engine fan containment applications. Int J Impact Eng 25(8):715–733

51. Wang CX et al (2019) High-velocity impact responses of 2618 aluminum plates for engine containment systems under combined actions of projectile form and oblique angle. Chin J Aeronaut 32(6):1428–1441

52. Liu LL et al (2017) Ballistic impact behaviour of stiffened aluminium plates for gas turbine engine containment system. Int J Crashworthiness 22(5):467–478

53. Roy PA, Meguid SA (2020) Modeling and characterization of bilayer containment ring in gas turbine engine. Int J Comput Methods Eng Sci Mech 21(2):96–108

54. Liu LL et al (2020) Ballistic impact performance of multi-phase STF-impregnated Kevlar fabrics in aero-engine containment. Thin-Walled Structures 157:14

55. Giannaros E et al (2021) Design by analysis of a multi-layer fabric reinforcement of jet engine containment for fragments mitigation. Compos Struct 275:13

56. Güden M et al (2023) Investigation and validation of the flow stress equation and damage model parameters of an electron beam melted Ti6Al4V alloy with a martensitic phase. Mater Sci Eng, A 885:145590

57. Sun G et al (2015) Evaluation of defect density, microstructure, residual stress, elastic modulus, hardness and strength of laser-deposited AISI 4340 steel. Acta Mater 84:172–189

58. Johnson GR (1983) A constitutive model and data for materials subjected to large strains, high strain rates, and high temperatures. Proc. 7th Inf. Sympo. Ballistics 541–547.

59. Johnson GR, Cook WH (1985) Fracture characteristics of three metals subjected to various strains, strain rates, temperatures and pressures. Eng Fract Mech 21(1):31–48

60. Lee W-S, Lin C-F (1998) High-temperature deformation behaviour of Ti6Al4V alloy evaluated by high strain-rate compression tests. J Mater Process Technol 75(1):127–136

61. Lee W-S, Lin C-F (1998) Plastic deformation and fracture behaviour of Ti–6Al–4V alloy loaded with high strain rate under various temperatures. Mater Sci Eng, A 241(1):48–59

62. Memu F et al (2019) Effect of surface roughness on tensile properties of electron beam melted Ti-6Al-4V alloy. in Euro PM 2019 Congress and Exhibition. European Powder Metallurgy Association (EPMA).

63. Tancogne-Dejean T, Spierings AB, Mohr D (2016) Additively-manufactured metallic micro-lattice materials for high specific energy absorption under static and dynamic loading. Acta Mater 116:14–28

64. Ansys/LS-DYNA, *LS-DYNA dev Keyword Manual Vol II – Material Models* 15 October 2024.

65. AASM Inc., https://www.aerospacemetals.com/asm-metal-distributor/.

66. Maxwell JC (1864) L On the calculation of the equilibrium and stiffness of frames. London Edinburgh Dublin Philos Mag J Sci 27(182):294–299

67. Deshpande VS, Ashby MF, Fleck NA (2001) Foam topology: bending versus stretching dominated architectures. Acta Mater 49(6):1035–1040